Electro-optical system for scanning microscopy of extreme ultraviolet masks with a high harmonic generation source

Patrick P. Naulleau,[1,*] Christopher N. Anderson,[1] Erik H. Anderson,[1] Nord Andreson,[1] Weilun Chao,[1] Changhoon Choi,[2] Kenneth A. Goldberg,[1] Eric M. Gullikson,[1] Seong-Sue Kim,[2] Donggun Lee,[2] Ryan Miyakawa,[1] Jongju Park,[2] Seno Rekawa,[1] Farhad Salmassi[1]

[1]*Center for X-ray Optics, Lawrence Berkeley National Laboratory, 1 Cyclotron Rd., Berkeley, California 94720, USA*

[2]*Samsung Electronics Co., Ltd., Hwasung, Gyeonggi 445-701, South Korea*

[*]*pnaulleau@lbl.gov*

Abstract: A self-contained electro-optical module for scanning extreme ultraviolet (EUV) reflection microscopy at 13.5 nm wavelength has been developed. The system has been designed to work with stand-alone commercially available EUV high harmonic generation (HHG) sources through the implementation of narrowband harmonic selecting multilayers and off-axis elliptical short focal length zoneplates. The module has been successfully integrated into an EUV mask scanning microscope achieving diffraction limited imaging performance (84 nm point spread function).

OCIS codes: (050.1965) Diffractive lenses; (110.0180) Microscopy; (110.7440) X-ray imaging; (340.7480) X-rays, soft x-rays, extreme ultraviolet (EUV).

References and links

1. S. Jeong, M. Idir, Y. Lin, L. Johnson, S. Rekawa, M. Jones, P. Denham, P. Batson, R. Levesque, P. Kearney, P. Yan, E. Gullikson, J. Underwood, and J. Bokor, "At-wavelength detection of extreme ultraviolet lithography mask blank defects," J. Vac. Sci. Technol. B **16**(6), 3430 (1998).
2. Y. Liu, A. Barty, E. Gullikson, J. S. Taylor, J. A. Liddle, and O. Wood, "A dual-mode actinic EUV mask inspection tool," Proc. SPIE **5751**, 660–669 (2005).
3. T. Haga, H. Takenaka, and M. Fukuda, "At-wavelength extreme ultraviolet lithography mask inspection using a Mirau interferometric microscope," J. Vac. Sci. Technol. B **18**(6), 2916 (2000).
4. K. Hamamoto, Y. Tanaka, S. Y. Lee, N. Hosokawa, N. Sakaya, M. Hosoya, T. Shoki, T. Watanabe, and H. Kinoshita, "Mask defect inspection using EUV microscope," J. Vac. Sci. Technol. B **23**(6), 2852 (2005).
5. K. Goldberg, P. Naulleau, A. Barty, S. Rekawa, D. Kemp, R. Gunion, F. Salmassi, E. M. Gullikson, E. H. Anderson, and H.-S. Han, "Performance of actinic EUVL mask imaging using a zoneplate microscope," Proc. SPIE **6730**, 67305E (2007).
6. T. Harada, J. Kishimoto, T. Watanabe, H. Kinoshita, and D. G. Lee, "Mask observation results using a coherent extreme ultraviolet scattering microscope at NewSUBARU," J. Vac. Sci. Technol. B **27**(6), 3203 (2009).
7. S. Lee, M. Guizar-Sicairos, and Y. Ekinci, "A novel concept for actinic EUV mask review tool using a scanning lensless imaging method at the Swiss Light Source," Proc. SPIE **9048**, 904811 (2014).
8. K. Goldberg, M. Benk, A. Wojdyla, I. Mochi, S. Rekawa, A. Allezy, M. Dickinson, C. Cork, W. Chao, D. Zehm, J. Macdougall, P. Naulleau, and A. Rudack, "Actinic mask imaging: Recent results and future directions from the SHARP EUV Microscope," SPIE **9048**, 90480Y (2014).
9. X-Ray Microscopy, Proceedings International Symposium, Goettingen, Germany, Sept, 14–16, 1983, edited by G. Schmahl and D. Rudolph Springer, Berlin, 1984, Vol. 43.
10. E.H. Anderson and D. Kern "Nanofabrication of Zone Plates for X-Ray Microscopy" in *X-Ray Microscopy III*, A. Michette, G. Morrison, and C Buckley, eds. (Springer Verlag, 1992).
11. E. H. Anderson, "Specialized electron beam nano-lithography for EUV and x-ray diffractive optics," IEEE J. Quantum Electron. **42**(1), 27–35 (2006).
12. W. Chao, T. Tyliszczak, J. Kim, P. Fischer, S. Rekawa, E. H. Anderson, "Latest development of ultra-high resolution soft x-ray zone plate microscopy" X-Ray Microscopy X (2010).
13. F. Brizuela, S. Carbajo, A. Sakdinawat, D. Alessi, D. H. Martz, Y. Wang, B. Luther, K. A. Goldberg, I. Mochi, D. T. Attwood, B. La Fontaine, J. J. Rocca, and C. S. Menoni, "Extreme ultraviolet laser-based table-top aerial image metrology of lithographic masks," Opt. Express **18**(14), 14467–14473 (2010).

#213528 - $15.00 USD Received 5 Jun 2014; revised 14 Jul 2014; accepted 15 Jul 2014; published 12 Aug 2014

14. B. A. Reagan, K. A. Wernsing, A. H. Curtis, F. J. Furch, B. M. Luther, D. Patel, C. S. Menoni, and J. J. Rocca, "Demonstration of a 100 Hz repetition rate gain-saturated diode-pumped table-top soft x-ray laser," Opt. Lett. **37**(17), 3624–3626 (2012).
15. X. Zhang, A. R. Libertun, A. Paul, E. Gagnon, S. Backus, I. P. Christov, M. M. Murnane, H. C. Kapteyn, R. A. Bartels, Y. Liu, and D. T. Attwood, "Highly coherent light at 13 nm generated by use of quasi-phase-matched high-harmonic generation," Opt. Lett. **29**(12), 1357–1359 (2004).
16. V. Tosa, H. T. Kim, I. J. Kim, and C. H. Nam, "High-order harmonic generation by chirped and self-guided femtosecond laser pulses. I. Spatial and spectral analysis," Phys. Rev. A **71**(6), 063807 (2005).
17. K. Midorikawa, "High-order harmonic generation and attosecond science," Jpn. J. Appl. Phys. **50**(9R), 090001 (2011).
18. B. Yoo, "EUVO: EUV light generation system," 2013 International Symposium on Extreme Ultraviolet Lithography, Toyama, Japan, October 6–10, 2013, proceedings available from SEMATECH, Albany, NY.
19 C. Jacobsen, S. Williams, E. Anderson, M.T. Browne, C. J. Buckleyc, D. Kern, J. Kira, M. Rivers, X. Zhang, "Diffraction-limited imaging in a scanning transmission x-ray microscope," Opt. Comm. **86**, 351 (1991).
20. T. Tyliszczak, T. Warwick, A. L. D. Kilcoyne, S. Fakra, D. K. Shuh, T. H. Yoon, J. G. E. Brown, S. Andrews, V. Chembrolu, J. Strachan, and Y. Acremann, "Soft x-ray scanning transmission microscope working in an extended energy range at the advanced light source," AIP Conf. Proc. **705**, 1356–1359 (2004).
21. P. P. Naulleau, I. Mochi, and K. A. Goldberg, "Optical modeling of Fresnel zoneplate microscopes," Appl. Opt. **50**(20), 3678–3684 (2011).
22. C. J. R. Sheppard and A. Choudhury, "Image formation in the scanning microscope," Opt. Acta (Lond.) **24**(10), 1051–1073 (1977).
23. H. Levinson, *Principles of Lithography 2nd Edition*, Chapter 8 (SPIE Press, 2005).
24. http://henke.lbl.gov/optical_constants/multi2.html
25. P. Naulleau, "The role of temporal coherence in imaging with extreme ultraviolet lithography optics," Opt. Commun. **219**(1-6), 57–63 (2003).
26. H. Levinson, *Principles of Lithography 2nd Edition,* Chapter 2 (SPIE Press, 2005).
27. S. Kim, D. Lee, J. Park, E. Kim, C. Jeon, H. Cho, B. Jeon, C. Choi, C. Anderson, R. Myakawa, and P. Naulleau, "EUV mask imaging system based on the scanning reflective microscopy," 2013 International Symposium on Extreme Ultraviolet Lithography, Toyama, Japan, October 6–10, 2013, proceedings available from SEMATECH, Albany, NY.

1. Introduction

The availability of actinic extreme ultraviolet (EUV) mask metrology tools remains a challenge for the commercialization of EUV lithography. To date, primarily only synchrotron-based tools have been available [1–8] with the most widely utilized tools relying on relatively simple and low cost Fresnel zoneplate optics [5,8–12].

Stand-alone Fresnel zoneplate tools based on plasma sources, EUV lasers [13,14], or high harmonic generation HHG sources [15–18] are all possible, but each system faces implementation challenges. Plasma-based systems are hampered by the temporal coherence requirements of zoneplates. EUV lasers meet the temporal coherence requirements of zoneplates, but none are currently available at the desired lithography wavelength of 13.5 nm. Moreover, the high spatial coherence of EUV lasers is not well suited for a full-field microscope. HHG sources are available at the correct wavelength, and have significantly better temporal coherence than plasma sources, but like EUV lasers, they are also spatially coherent.

While spatial coherence is a problem for full-field imaging, it is actually ideal for scanning microscopy, a technique widely used in the synchrotron community [19,20]. In addition to being well suited for HHG sources, scanning geometries have the added benefit of overcoming field size limitations of zoneplates [21]. A potential problem with scanning systems, however, is that its imaging performance is directly limited by the wavefront quality of the source itself as well as all the illumination optics upstream of the zoneplate. Given that the wavefront quality of HHG sources is determined by the wavefront quality of the much longer driving wavelength, very high quality (λ/40 or better) is possible [18].

Figure 1 shows a schematic diagram of a scanning microscope as might be implemented for the inspection of EUV masks. Shown is the heart of the microscope which is an electro-optical system that collects and filters the light, focuses it, and then detects it. The angles are exaggerated and components are not to scale for illustrative purposes. The operating wavelength is 13.56 nm and the beam size on the turning mirror is on the order of 500 μm in diameter. The zoneplate is positioned approximately 550 μm above the surface of the mask and the order sorting aperture is about 100 μm above the mask (to scale details of the

#213528 - $15.00 USD Received 5 Jun 2014; revised 14 Jul 2014; accepted 15 Jul 2014; published 12 Aug 2014

zoneplate and order sorting aperture are shown in Fig. 6). The detector is a single element photodiode placed at a distance of approximately 75 mm and has an active diameter of approximately 11 mm. The only moving part in this system is the mask itself which is scanned under the beam to form the image and is moved in height to adjust focus. In this paper we describe the design, implementation, and testing of such a system, demonstrating diffraction limited performance.

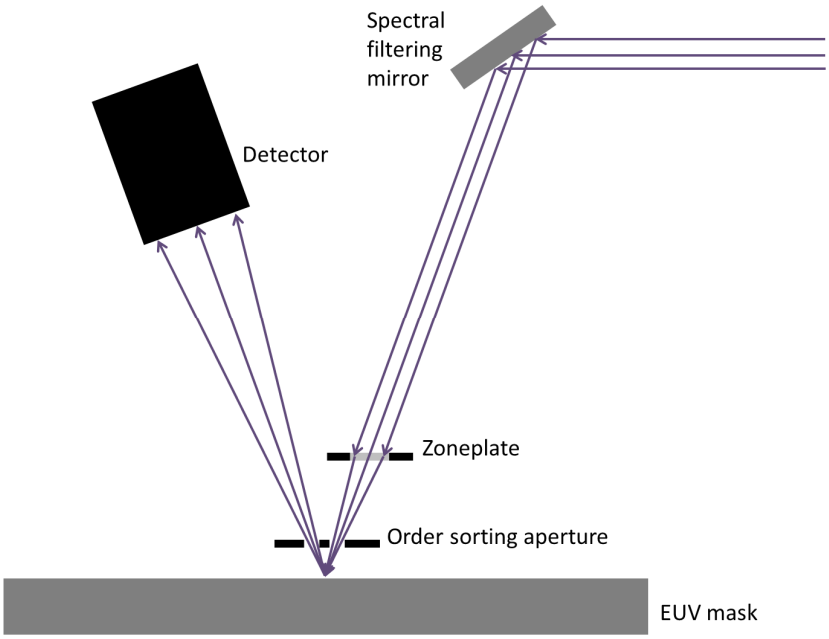

Fig. 1. Schematic of scanning microscope for the inspection of EUV masks.

2. System design

The goal of the optical system described here is to mimic the mask side imaging properties of an EUV lithography tool with a numerical aperture (NA) of 0.33. As depicted in Fig. 1, coherent light is collected by a turning mirror and directed to a zoneplate which focuses the beam onto the mask. The beam strikes the mask at the same angle of incidence as in the lithography tool. The reflected intensity within the acceptance angle of the detector is then measured. A full two dimensional image is formed by scanning the mask under the beam and recording the reflected intensity at each point on the mask. Despite operating with fully coherent light, the system in Fig. 1 can mimic the performance of any partial coherence imaging system by control of the detector aperture [22]. In such a system the detector angular aperture becomes fully equivalent to the condenser aperture in a conventional imaging system. Thus when the acceptance angle of the detector is set to match the NA of the focusing zoneplate, we have a partial coherence factor (or sigma) of 1. More restrictive apertures will cause the sigma to decrease and thus the imaging properties to become more coherent. We note thus this equivalence is not limited to on axis apertures, but also holds for any illumination type such as dipole, quadrupole, etc [23]. The role of the lithographic imaging optic is fulfilled by the focusing zoneplate which has the same NA as the mask side of the lithography tool, or 0.33/4 = 0.0825 since the magnification of the lithography tool is 4.

In addition to the spatial coherence, another technical difference between the system described here and the true lithographic system is spectral bandwidth. As described below, use of a diffractive optic places more stringent spectral constraints on the source compared to

#213528 - $15.00 USD Received 5 Jun 2014; revised 14 Jul 2014; accepted 15 Jul 2014; published 12 Aug 2014

the typical 2% bandwidth passed by a multilayer reflective system [24]. It has been shown that even at 2% bandwidth, an EUV lithography system is quasi-monochromatic and thus has the same imaging characteristics as narrower band systems such as the one described here [25]. We note, however, that this equivalence would break down as the bandwidth is increased such that chromatic aberrations in the zoneplate can no longer be ignored as might be the case if one is trying to increase the bandwidth to achieve increased optical throughput.

3. Harmonic selecting mirror

The first optical component in the imaging system is the harmonic selecting fold mirror. In the system described here, the angle of incidence on this fold mirror is 48° relative to normal incidence. As demonstrated in Fig. 2, trying to use a conventional multilayer in this case would cause significant problems since three harmonics would be well reflected by the mirror. The reflectivity curve shown in Fig. 2 was computed using the Center for X-Ray Optics website [24] and assumes and ideal Mo/Si mirror. The harmonic wavelengths are computed assuming a HHG drive wavelength of 800 nm. Assuming a zoneplate focal length of 500 μm, the harmonics at 13.11 nm and 14.04 nm would produce images with 16 and 18 Rayleigh units [26] of defocus respectively.

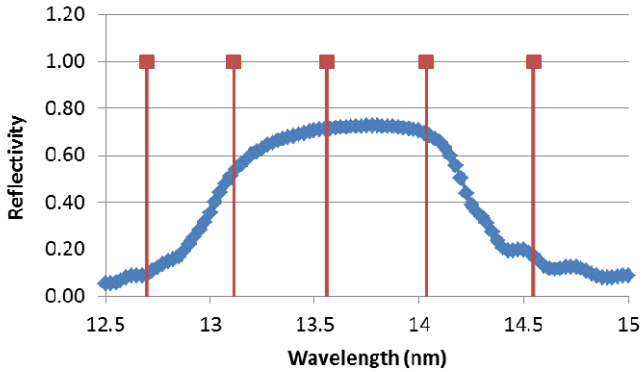

Fig. 2. Comparison of HHG harmonics and conventional turning mirror bandwidth.

Even if a single harmonic is considered, when using diffractive lenses we must also be concerned with the intrinsic bandwidth of the harmonic itself, which can vary as a function of source parameters. For the application described here, it is evident that narrower band multilayers are required. Narrow bandwidth, however, comes at the cost of reflectivity. Figure 3 shows results from a study performed using the magnetron coating facility at the Center for X-ray Optics determining the impact of coating full-width half maximum (FWHM) spectral resolution on peak reflectivity for 45° Mo/Si turning mirrors. At 45° angle of incidence, a maximum FWHM spectral resolution $\lambda/\Delta\lambda$ of close to 100 is achieved. The measurements were performed using the Center for X-ray Optics Calibrations and Standards beamline at the Advanced Light Source synchrotron facility.

The HHG source used in the application described here [18] has been demonstrated to have a FWHM spectral resolution $\lambda/\Delta\lambda$ of 280, requiring only harmonic selection from the multilayer and not additional harmonic narrowing. Figure 4 shows the reflectivity curve for the harmonic selecting mirror we used along with the locations of the harmonics. This is one of the mirrors from the set shown in Fig. 3. The mirror has a peak reflectivity of 42% and a spectral resolution of $\lambda/\Delta\lambda$ of approximately 46. Despite the reflectivity being non-zero at the adjacent harmonics, modeling (beyond the scope of this paper) shows that suitable imaging performance can still be achieved. The large defocus these harmonics suffer leads to these components simply adding low level DC background.

#213528 - $15.00 USD Received 5 Jun 2014; revised 14 Jul 2014; accepted 15 Jul 2014; published 12 Aug 2014

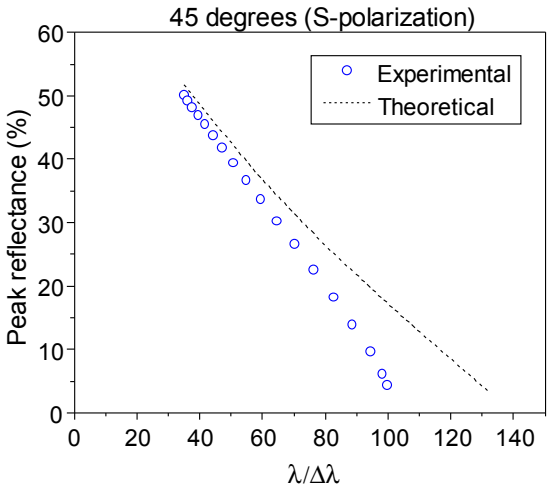

Fig. 3. Peak reflectance as a function of bandwidth. The dotted line shows predicted results for an ideal system and the blue circles show measured results for the magnetron coated samples.

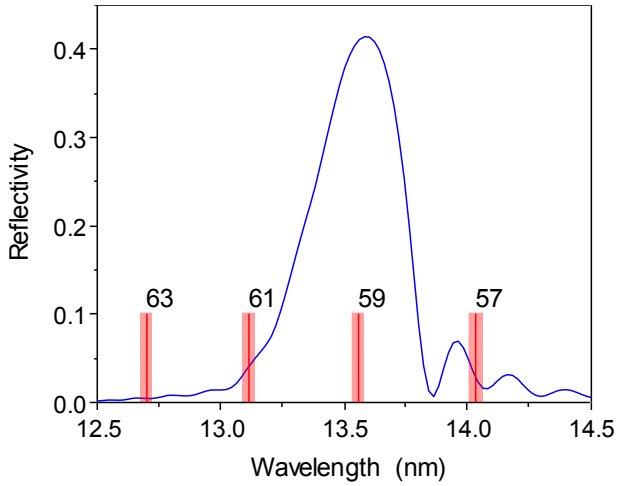

Fig. 4. Reflectivity vs wavelength for the chosen harmonic selecting mirror with a peak reflectivity of 42% and resolving power of 46.

4. Zoneplate lens

Despite the HHG source used here having quite narrow bandwidth, the bandwidth still remains large relative to values obtained in synchrotron applications which are typically λ/Δλ of 1000 or better. The implication of this constraint is that the zoneplate focal length must be limited. Defining the chromatic defocus range and the change in zoneplate focal length over the full bandwidth, this range can readily be shown to be directly proportional to focal length. Assuming a bandwidth λ/Δλ of 280 and a NA of 0.0825 (0.33/4), Fig. 5 shows the computed chromatic defocus range in Rayleigh units as a function of focal length. Limiting the system to about 2 Rayleigh units of focal range sets an upper bound on the focal length of about 550 μm.

#213528 - $15.00 USD Received 5 Jun 2014; revised 14 Jul 2014; accepted 15 Jul 2014; published 12 Aug 2014

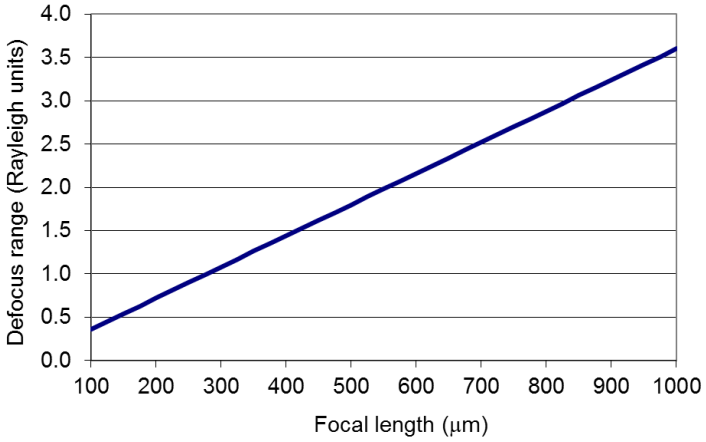

Fig. 5. Computed chromatic defocus range in Rayleigh units as a function of focal length assuming λ/Δλ of 280 and NA of 0.0825 (0.33/4).

With such tight focal length constraints and the further requirement for an order sorting aperture close to focus, it becomes impractical to mount the zoneplate perpendicular to the optical axis, but rather it must be mounted parallel to the object (mask) plane which in this case is tilted at 6° from normal to the optical axis. A schematic showing the geometry of the zoneplate region is shown in Fig. 6. The incidence angle has been exaggerated from the actual value of 6° to 12° in the schematic for improved visualization. The optical parameters for this example zoneplate are shown in Table 1.

Table 1. Example Zoneplate Optical Parameters

Parameter	Value
Diameter	90.75μm
Angle of incidence	6°
Wavelength	13.5 nm
Focal length	550 μm
Zone material	Ni
Zone thickness	80 nm
Outer zone width	82 nm
NA	0.0825
Number of zones	277

Note that our requirement that the chromatic defocus range be less than 2 Rayleigh units has led to a number of zones that is consistent with the rule of thumb stating that the number of zones should be less than or equal to λ/Δλ.

The problem with the geometry shown in Fig. 6 is that at an angle of incidence of 6° on a conventional zoneplate, significant wavefront aberrations would be expected. For this case, it can be shown that one would expect more than 1 wave of astigmatism and nearly ½ wave of coma, which would lead to unacceptable imaging performance. This problem, however, can be eliminated by specific design of the zoneplate. A zoneplate can be generally viewed as the hologram formed by a pair of point sources: one at the target object point and a second at the target image point. From this perspective, the ideal zoneplate for the target geometry described above can be determined by computing the interference pattern that would result from two on-axis source points, one at a distance of 1 m (the distance to the source) and a second at a distance of 550 μm (the distance to the sample plane), but the fringe computation plane should be tilted by 6° relative to the optical axis (Fig. 7). In general, this will produce a zoneplate of slightly elliptical shape.

At 6°, the elliptical shape is very subtle (<0.6%) and cannot be perceived by eye as demonstrated by the scanning electron micrograph of the zoneplate along with the adjacent

#213528 - $15.00 USD Received 5 Jun 2014; revised 14 Jul 2014; accepted 15 Jul 2014; published 12 Aug 2014

return hole shown in Fig. 8. The spurious circular patterns observed in the zoneplate are simply Moiré artifacts in the image. Based on the computed aberrations (~1 wave) for a conventional zoneplate described above, one would expect the magnitude of the correction to be only on the order of one zone pair at the edge of the zoneplate or approximately 160 nm.

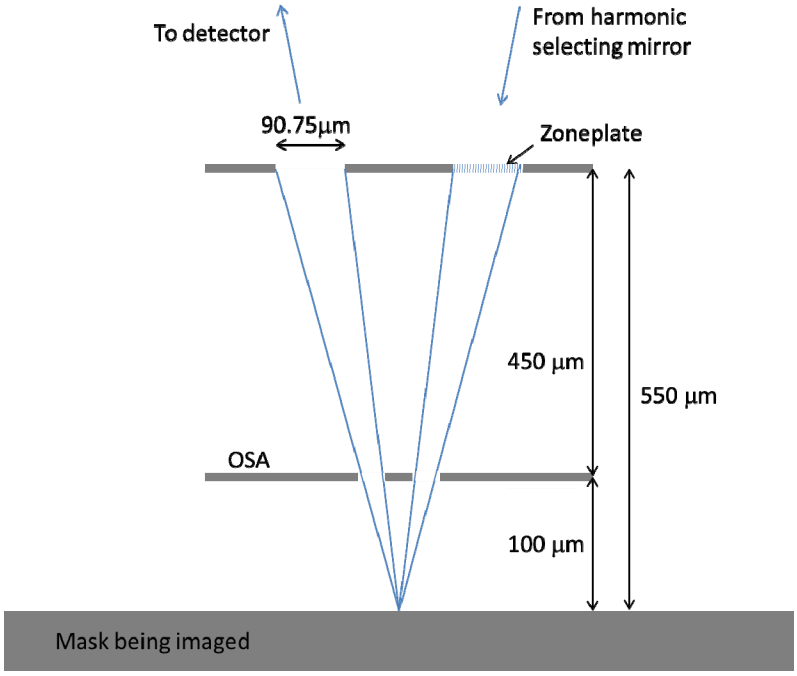

Fig. 6. Schematic showing the geometry of the zoneplate region. The incidence angle is exaggerated from actual value of 6° to 12° in schematic for improved visualization.

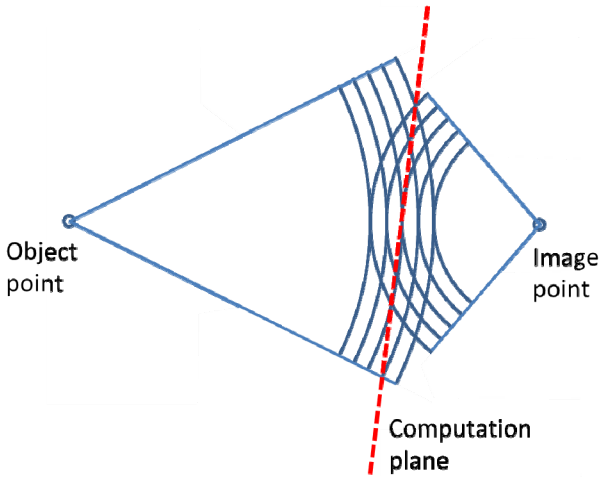

Fig. 7. Computation geometry for tilted zoneplate.

#213528 - $15.00 USD Received 5 Jun 2014; revised 14 Jul 2014; accepted 15 Jul 2014; published 12 Aug 2014

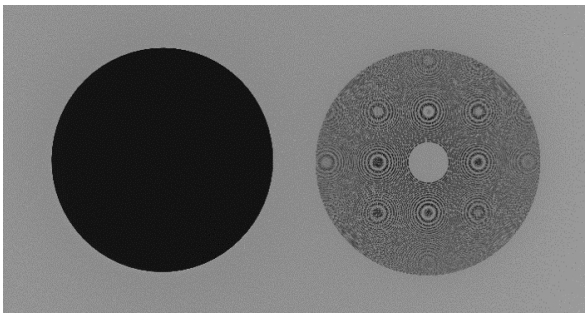

Fig. 8. Scanning electron micrograph of zoneplate along with adjacent return hole. The extra circular patterns observed in the zoneplate are Moire artifacts.

Alignment of the OSA to the zoneplate is crucial to system performance and given the tight geometry it is particularly challenging. To address this concern, microfabrication techniques have been employed to ensure that the components can be accurately and kinematically aligned. The zoneplate and OSA are fabricated onto separate silicon chips which also include lithographically defined V-grooves. Precision sapphire balls are then placed into the V-grooves and used to couple the chips together. The lithographic process ensures the lateral positioning accuracy and the ball diameter and groove depth ensure the longitudinal accuracy. A photograph of a completed zoneplate/OSA assembly is shown in Fig. 9. The OSA chip (top) seemingly floating above the zoneplate chip is actually supported by the 3 sapphire balls.

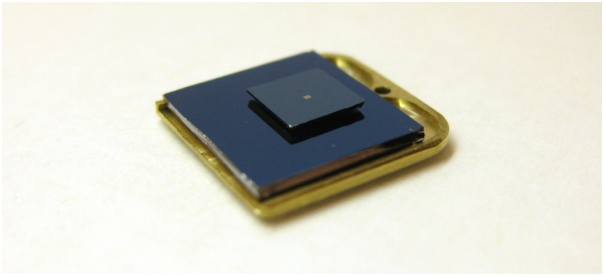

Fig. 9. Photograph of zoneplate/OSA assembly. The OSA chip (top) seemingly floating above the zoneplate chip is actually supported by 3 sapphire balls.

5. Detector

As described above, the detector is a single element photodiode which must separately record each pulse from the 1kHz source. The detector is positioned approximately 100 mm from the mask and has an active diameter of approximately 17 mm. To achieve low noise performance, a pre-amp is directly coupled to the detector housing in vacuum. A second amplifier is then placed outside of vacuum and the signal is routed into pulse shaping and peak holding electronics before analog to digital conversion. The target electronic noise limits are set based on the expected photon count of 4000 photons per pulse from a bright region on the mask. Setting the detector noise limit to ½ the photon limit (63 photons) and noting a detector electron yield of 20 electrons per photon, a target electrical noise limit of 600 electrons is determined. Electrical tests on the final detector and electronics package have demonstrated a noise floor of 400 electrons.

Another concern for the detector is sensitivity to out of band light. In particular, for the HHG source, 800-nm light must be suppressed. This can readily be achieved using a zirconium filter mechanically coupled to the detector. To this end, we fabricated a 400-nm thick zirconium membrane bonded to an aluminum ring (Fig. 10). The filter provides 20% EUV transmission and 10^{12} suppression of 800-nm light. Also seen in Fig. 10 is the

#213528 - $15.00 USD Received 5 Jun 2014; revised 14 Jul 2014; accepted 15 Jul 2014; published 12 Aug 2014

complementary component to the OSA fabricated into copper by laser milling. The 1-mm disk on the optical axis blocks on-axis zero-order light making it through the zoneplate packaged OSA as well as light reflected off the back surface of the zoneplate.

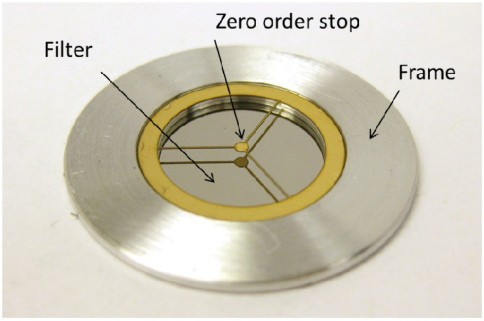

Fig. 10. Photograph of zirconium filter and zero-order stop assembly.

6. Assembly

A significant benefit of the simple optical configuration of the system described here is in the relatively relaxed alignment tolerances it affords. From the aberration perspective, the only alignment parameters that matter are the angular orientations of the zoneplate relative to the beam. Table 2 shows the induced astigmatism, coma, and spherical aberration as a function of pitch, roll, and yaw alignment error. Note that these alignment errors do not add any spherical aberration. Spherical error would be expected for an error in the conjugate distances, but given the extremely large demagnification and object distance, conjugate distance error is not a concern here. Limiting the alignment error to $\lambda/40$ sets an angular tolerance of 0.1 degrees for pitch and roll and 1 degree for yaw.

The tolerances described above are all well within precision machining capabilities, thus we choose to build a single monolithic structure with the required reference surfaces for the turning mirror, zoneplate assembly, and detector assembly (Fig. 11). For enhanced stability, the structure is machined into low expansion glass. Fabrication of the housing was performed by Zygo Extreme Precision Optics.

Table 2. Angular Alignment Tolerances

Alignment sensitivity (waves/deg)			
Aberration	**Alignment error orientation**		
Type	**Pitch**	**Roll**	**Yaw**
Astigmatism	0.229	0.229	0.024
Coma	0.059	0.059	0.006
Spherical	0.000	0.000	0.000

7. Imaging performance

The system described above has been integrated into a complete EUV mask imaging microscope (Fig. 12) by Samsung Semiconductor [27]. The system uses a commercially available HHG source [18]. Lateral shearing interferometry was used to measure the wavefront quality from which we compute the point spread function shown in Fig. 13. Figure 14(a) shows an image of 100-nm lines and spaces on the mask (corresponds to 25-nm wafer dimensions in use). Figure 14(b) shows 120-nm contacts (30-nm at the wafer). The scan step size is 20 nm and the single frame exposure time is approximately 4 seconds. Finally, Fig. 14 shows an image of an example EUV-specific defect on the mask compared to an actual wafer print with the mask and a scanning electron micrograph of the mask. As expected, EUV microscope image shows good correlation to EUV printing results.

#213528 - $15.00 USD Received 5 Jun 2014; revised 14 Jul 2014; accepted 15 Jul 2014; published 12 Aug 2014

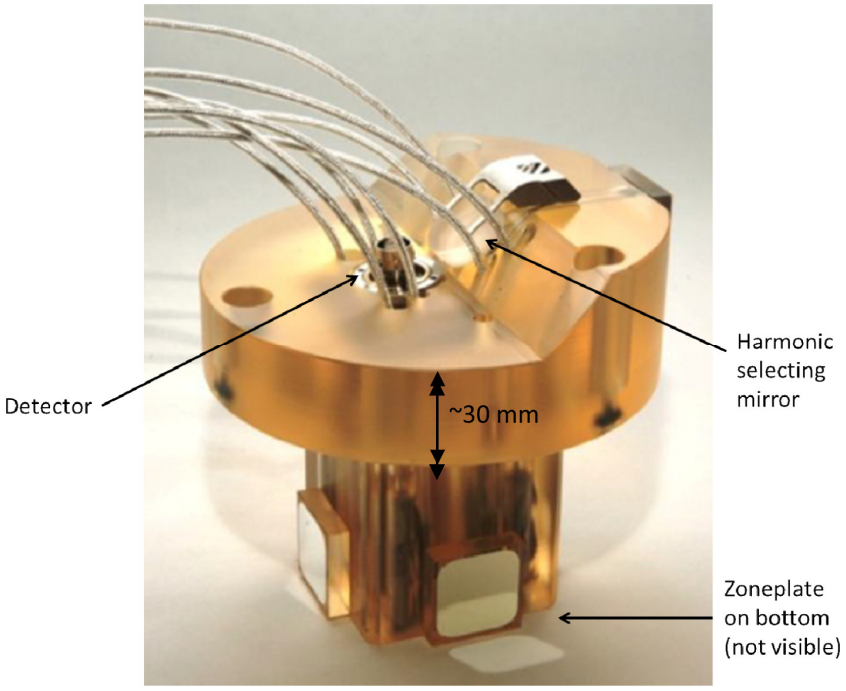

Fig. 11. Photograph of complete assembly.

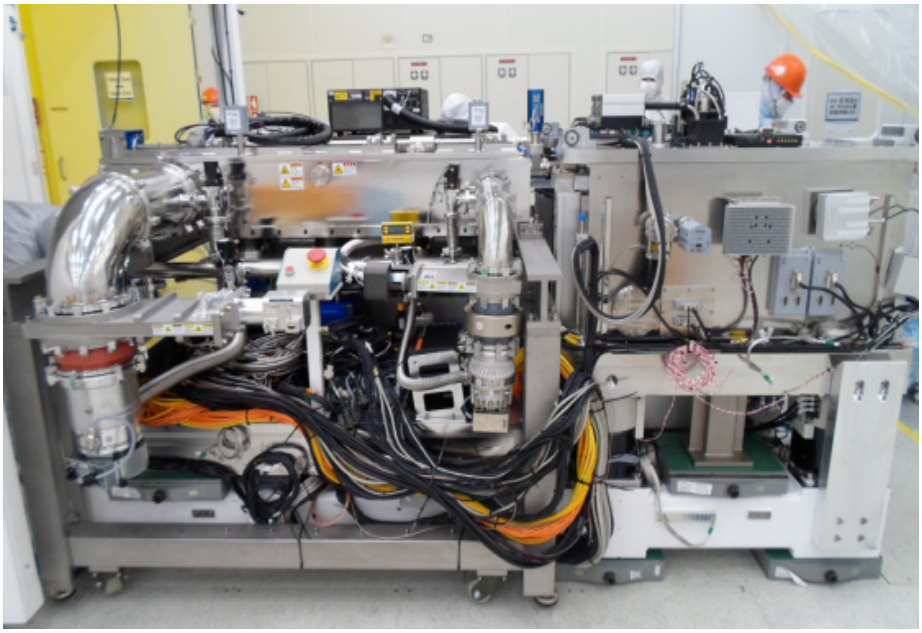

Fig. 12. Photograph of fully integrated EUV scanning microscope.

#213528 - $15.00 USD Received 5 Jun 2014; revised 14 Jul 2014; accepted 15 Jul 2014; published 12 Aug 2014

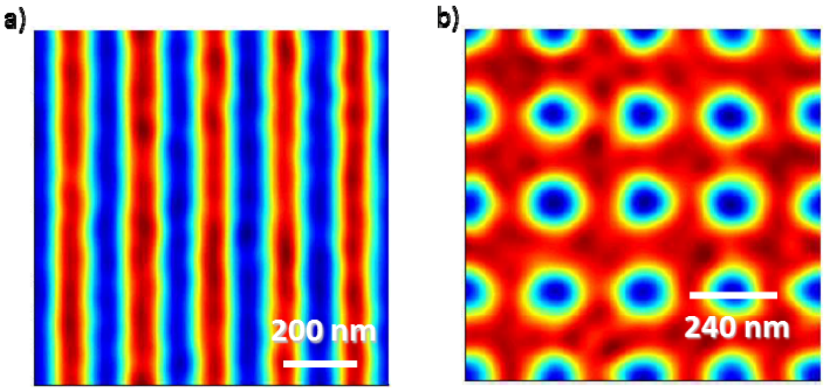

Fig. 13. EUV mask images recorded using the optical system described here and integrated into an EUV scanning microscope at Samsung Semiconductor. a) 100-nm lines and spaces on the mask corresponding to 25-nm wafer dimensions when mask is in use. b) 120-nm contacts corresponding to 30-nm features on wafer.

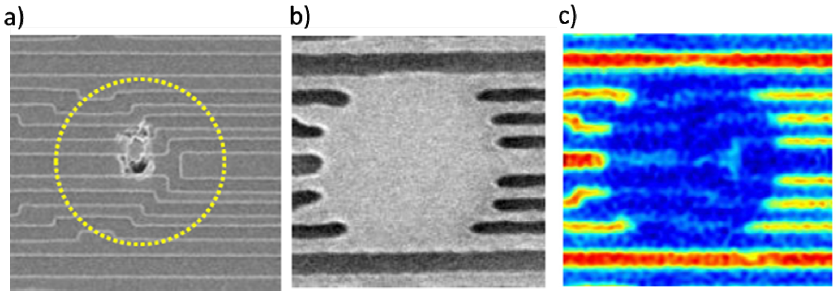

Fig. 14. Images of EUV-specific defect on mask demonstrating importance of EUV metrology. a) Scanning electron microscope image of mask, b) Scanning electron microscope image of EUV wafer print using the mask, and c) EUV scanning microscope image.

8. Summary

A self-contained electro-optical module for scanning EUV reflection microscopy has been developed. The system uses a harmonic selecting multilayer and off-axis short focal length zoneplate designed to work with stand-alone commercially available EUV HHG sources. The module has been successfully integrated into an EUV mask scanning microscope achieving diffraction limited performance (84 nm FWHM).

Acknowledgments

This work was supported by Samsung Semiconductor through the U.S. Department of Energy under Contract No. DE-AC02-05CH11231.

#213528 - $15.00 USD Received 5 Jun 2014; revised 14 Jul 2014; accepted 15 Jul 2014; published 12 Aug 2014